Numerical Study of Particle Impingement on Aeroengine under Mixed-Phase Conditions

Qilei GUO*, Jie DU**, Feng QIAN***, Ning DING****

*Civil Aviation Flight University of China, Guanghan 618307, China, E-mail: guoql@cafuc.edu.cn
**Civil Aviation Flight University of China, Guanghan 618307, China, E-mail: cafuc_dujie@outlook.com
***Civil Aviation Flight University of China, Guanghan 618307, China, E-mail: QianF@cafuc.edu.cn (Corresponding author)
****Civil Aviation Flight University of China, Guanghan 618307, China, E-mail: DingNing135@outlook.com

1. Introduction

Interest in ice crystal icing has intensified following the recognition of its significant threat to aviation safety, particularly concerning contemporary turbofan engines which ingest minute ice crystals [1]. Since the 1990s, instances of power reduction in high-bypass ratio engines operating above 7,000 meters, where supercooled liquid droplets are scarce, have multiplied. Large amounts of investigations shown that the cause of the accident is that the ice crystals inhaled by the engine partially melt on the surface of inner channel components, and further freeze [2, 3].

When an aircraft is cruising at high altitudes to shelter from rainfall, the engines may suck in large amounts of ice crystals. Under the action of the high temperature internal flow of the engine, these ice crystals will partially melt, creating a mixed phase of ice and water. The ice-water mixed phase particles will further transform to a liquid water film on the surface of the internal structure of the engine such as the compressor blades, and subsequently inhaled ice crystals will adhere to these wet surfaces and cool the surface temperature to below the freezing point. As ice crystal intake persists, ice will eventually accumulate on the surface of the inner structure. Distinct from exterior icing caused by the impact of supercooled water droplets, ice crystal icing may span from the low-pressure compressor to the high-pressure compressor's initial stator vane. This phenomenon can instigate engine surges, stalls, or catastrophic structural failures linked to ice shedding [4].

Scholars have carried out in-depth research on the freezing mechanism of ice crystals by ground tests and numerical simulations. In terms of experimental research, Struk [5], Currie [6] and others believe that the wet bulb temperature T_{wb} can be used as the criterion for judging whether the icing is stable, that is when $T_{wb}<0°C$, the wetted surface can generate stable icing. Currie et al. [7] described the ice accretion process with the adhesion efficiency, and discussed the effect of Melt Ratio (MR) and impact angle on the adhesion efficiency. Al-Khalil et al. [8] conducted experiments on ice crystal freezing under rime ice and glazed ice conditions, respectively, and found that the impact of ice crystals would weaken the ice crystal freezing. Knezevici et al. [9] further found that affecting by crystals of varying sizes, ice crystal erosion diminishes accretion. Hauk [10, 11] delved into the characteristics and influencing variables governing the impact of spherical and irregularly shaped ice crystals.

While simulated icing experiments on aero-engines provide invaluable insights, they are hindered by high costs, protracted timelines, and limited generalizability. Therefore, the numerical method has also emerged as an important tool for probing ice crystal freezing mechanisms. Villedieu et al. [12] applied the Lagrangian approach to model mathematical models for ice crystal shape, thermodynamics, phase transition, and surface interactions, such as adhesion, fragmentation, rebound and splashing, during impacting. On this basis, Trontin et al. [13] refined the adhesion model of ice crystals by considering erosion effects, validating the empirical parameters in numerical models against experimental outcomes. Further numerical simulations were carried out under various icing conditions of supercooled large droplets, ice crystals and mixed-phase [14]. Norde et al. [15] employed the Euler method for particle trajectories calculation and advanced the Messinger thermodynamic icing model according to the characteristics of the mixed-phase heat and mass transfer process. Zhang et al. [16] established an ice crystal impact model by comprehensively considering the splashing of droplets and the breakage and rebound of ice crystals, and further proposed a mixed phase icing thermodynamic model. Bu et al. [17] numerically studied mixed-phase icing on the NACA0012 aerofoil, considering the ice crystal adhesion effect, and found the adhesion effect has a significant influence on the amount of ice and ice shape. Qi et al. [18] numerically studied the characteristics of mixed phase ice accretion in aero-engines and investigated the sensitivity parameters of ice accretion. Currie [19], Baumert [20], Bartkus [21] respectively calibrated and improved their owned numerical calculation codes for ice crystal icing in accordance with ice wind tunnel test datasets.

In this paper, considering the ice crystal sticking effects, a numerical model grounded in the Euler method to analyse particle impingement characteristics within a large bypass ratio aeroengine under mixed-phase icing conditions is introduces. Mass flux, film thickness and adherence fractions across various melt ratios are examined, thereby the mechanism of liquid films in modulating ice crystal adhesion dynamics is analysed.

2. Mathematical Modelling

2.1. Air flow field model

The air flow field is modeled by the conservation of mass, momentum and energy. For a compressible flow,

the density of the fluid is no longer considered to be a linear function of pressure and velocity. For rotating components, aforementioned equations are converted to the relative frame of reference to account for the rotational speed. Therefore, the mass conservation can be calculated as follows:

$$\frac{\partial \rho_a}{\partial t} + \nabla\left(\rho_a \boldsymbol{u}_r\right) = 0 \,, \tag{1}$$

where ρ_a and $\boldsymbol{u}_r$ are respectively the density and velocity vector of air, and the subscript r represents the relative reference frame.

The momentum conservation demonstrates that the total force acting on a fluid particle is equal to the time rate of change of its momentum. It can be written in 3D using 3 non-linear equations, shown here in vector form:

$$\frac{\partial \rho_a \boldsymbol{u}_r}{\partial t} + \nabla\left(\rho_a \boldsymbol{u}_r \boldsymbol{u}_r\right) = \nabla \tau + \rho_a \boldsymbol{g} + F_{ext} \,. \tag{2}$$

Here τ is the stress tensor and $\boldsymbol{g}$ is the acceleration of gravity. The external force vector F_{ext} in above equations consist of the Coriolis force, F_{cor}, and centrifugal force, F_{cen}:

$$F_{ext} = F_{cor} + F_{cen} = -2\rho_a\left(\boldsymbol{n}\times\boldsymbol{u}_r\right) - \rho_a\boldsymbol{n}\times\left(\boldsymbol{n}\times\boldsymbol{r}\right). \tag{3}$$

Here n is the rotational velocity of the component and r is the distance from the axis of rotation.

The conservation of energy states that the total energy of the system must be conserved. The energy equation for rotating components is:

$$\frac{\partial \rho_a E_r}{\partial t} + \nabla\left(\rho_a \boldsymbol{u}_r H_r\right) = \nabla\left(\kappa_a\left(\nabla T_a\right) + \boldsymbol{u}_r\tau\right), \tag{4}$$

where E_r and H_r are the relative internal energy and total enthalpy. E_r and H_r can be calculated as follows:

$$\begin{aligned} E_r &= e + \frac{1}{2}\left(\boldsymbol{u}_r^2 - \boldsymbol{u}_t^2\right), \\ H_r &= h + \frac{1}{2}\left(\boldsymbol{u}_r^2 - \boldsymbol{u}_t^2\right). \end{aligned} \tag{5}$$

Here, $\boldsymbol{u}_r$ is the relative velocity in the rotating frame and $\boldsymbol{u}_t$ is the tangential velocity of the rotating frame, which is calculated as $\boldsymbol{n}\times\boldsymbol{r}$. And κ_a is the thermal conductivity, which is computed in a similar way to the laminar dynamic viscosity.

$$\kappa_a = C1*\left(T_a^{3/2}\right)/\left(T_a + 133.7\right), \tag{6}$$

where T_a refers to the static air temperature in Kelvin and $C1$ is a constant.

2.2. Mixed phase trajectory equations

The general Eulerian two-fluid model consists of the Euler or Navier-Stokes equations augmented by the mass and momentum equations. For rotating components, the Eulerian equations are modified to include the rotational body forces. Therefore, these equations can be calculated as

follows:

$$\frac{\partial \alpha}{\partial t} + \nabla\left(\alpha u_{r,p}\right) = 0 \,, \tag{7}$$

$$\begin{aligned} &\frac{\partial\left(\alpha u_{r,p}\right)}{\partial t} + \nabla\left(\alpha u_{r,p} u_{r,p}\right) = \\ &= \frac{C_d\, Re_p}{24K}\left(u_a - u_p\right) + \frac{\alpha}{Fr^2}\left(1 - \frac{\rho_a}{\rho_p}\right)g + F_{ext}\,, \end{aligned} \tag{8}$$

where α and $u_{r,p}$ refer to the particle concentration and the particle velocity relative to the frame of reference, K is particle inertia parameter, C_d is the drag coefficient of the mixed phase, Fr is the Froude number, u_a and u_p are the velocity of the air and particle. It is noted that p can be replaced by d or ic to respectively represent droplets or ice crystals in mixed phase.

The calculation of F_{ext} can refer to Eq. (3), but note that $\boldsymbol{u}_r$ should be replaced by the particle velocity, $\boldsymbol{u}_{r,p}$. And particle Reynolds number Re_p are defined as

$$Re_p = \frac{\rho_a d_p u_a \left\|u_a - u_p\right\|}{\mu_a}\,, \tag{9}$$

Supercooled droplets or crystals entering a turbomachine warm up progressively, but not at the same rate as the airflow. In this manner, the temperature difference between the particle and the surrounding airflow increases as particles travel through the compressor. The particle energy equation is:

$$\frac{\partial E}{\partial t} + \frac{\partial\left(vE\right)}{\partial x} = \dot{S}\,, \tag{10}$$

where the source term $\dot{S}$ accounts for the energy transfer between the mixed phase and the airflow. The term $\dot{S}$ can be sub-divided to include terms such as convection with airflow ($\dot{q}_{conv}$), absorption or emission due to radiant energy ($\dot{S}_{rad}$), and addition or losses due to mass coupling effects that cause evaporation/condensation ($\dot{q}_{evap/cond}$), freezing or melting ($\dot{q}_{freeze/melt}$). The source term is expressed as follow:

$$\dot{S} = \alpha\left(\dot{q}_{conv} + \dot{S}_{rad} + \dot{q}_{evap/cond} + \dot{q}_{freeze/melt}\right). \tag{11}$$

In Eq. (10), E represents the total internal energy of the mixed phase and is calculated as follows:

$$E = \alpha i \,. \tag{12}$$

Here i is the specific internal energy of the particle. For ice crystals, the temperature is obtained directly from the specific internal energy of ice crystals

$$i = i_{ref} + c_{p,ice}\left(T - T_{ref}\right) - L_{fussion}\,, \tag{13}$$

where $c_{p,ice}$ is the isobaric specific heat capacity of the ice crystals, $L_{fussion}$ is the latent heat of fusion to melt ice crystals and given to 333,000 J/kg/k, i_{ref} and T_{ref} refer to reference specific internal energy and reference temperature.

Due to the sublimation and evaporation of ice crystals, the vapor transport equation is introduced and it is calculated as follows [18]:

$$\frac{\partial \alpha_{vap}}{\partial t} + \nabla \left(\alpha_{vap} u_{r,a} \right) = \nabla \left(D_{eff} \nabla \alpha_{vap} \right) + S \qquad (14)$$

where α_{vap} and $\boldsymbol{u}_{r,a}$ refer to the vapor concentration and the air velocity relative to the frame of reference, S is volumetric mass flux source that represents vapor condensation, droplet evaporation or crystal sublimation. D_{eff} is the effective mass diffusion coefficient that combines laminar diffusion coefficient, D_1, and turbulent diffusion coefficient, D_t. It can be calculated as follows: $D_{eff} = D_l + D_t$. The latter is calculated as follows:

$$D_t = \left(\rho S c_t \right) / \mu_t , \qquad (15)$$

here μ_t is the turbulent viscosity and Sc_t is the turbulent Schmidt number.

2.3. Crystal sticking model

Under normal circumstances, it is hypothesized that the supercooled liquid droplets will all adhere in the icing process after impacting the icing surface. However, different from supercooled liquid droplets, ice crystals may break, bounce or stick to the surface when impacting on the surface. Experiments of ice crystal impact on the surface of NACA0012 airfoil by Baumert et al. [20] shown that the rebounded particles rarely impact the wall again except near the stagnation point, which has little effect on the icing process.

Therefore, the main concern in mixed-phase icing conditions is on the adhesion effect of ice crystals. Nilamdeen et al. [22] defined the adhesion coefficient based on the Euler method and pointed out that the kinetic behavior of ice crystal impact is affected by parameters such as ice crystal particle size, impact velocity, and liquid film thickness. In the literature, it assumed that all ice crystals rebound in the rime icing area, and all ice crystals adhere in the liquid film area, that is, the adhesion coefficients are $\varepsilon_{st} = 0$ and $\varepsilon_{st} = 1$ respectively. While in the glazed ice area, the ice crystal adhesion coefficient is related to the impact speed of ice crystals and liquid film thickness, and complies the following relationship:

$$\varepsilon_{st} = \frac{h_f}{max\left(h_f \right)} \frac{1}{exp\left(\chi \|v_n\|^2 \right)} , \qquad (16)$$

where ε_{st} is assumed to be linearly proportional to the ratio of h_f and maximum film height calculated $max(h_f)$ and inversely proportional to the normal impact velocity v_n. The parameter χ controls the limit of v_c beyond which no crystals stick and is obtained using the following equation and assuming $h_f = h_{f,\,max}$ and $\varepsilon_{st} = \Psi$, where Ψ is a very small number:

$$\chi = \frac{1}{v_n^2} ln\left(\frac{1}{\Psi} \right) . \qquad (17)$$

Here, all particles that exceed v_c are assumed to bounce without sticking, with v_c defined as $v_n = 2/d_p$, d_p is the diameter of ice crystal.

3. Case Study

In this paper, a large bypass ratio engine is taken as the research object, which includes the nose cone, fan blade, guide vane in bypass duct and guide vane in core duct. The assembly drawing of the aero engine components is demonstrated in Fig. 1, a and the corresponding grid model is shown in Fig. 1, b. Due to the number of fan blades and guide vanes is different, the above components are modelled separately. After the mesh refinement, the number of assembled mesh model is about 1.2 million structural grids. The inlet and outlet boundary conditions adopt the mass flow inlet and subsonic outlet, respectively, and the data exchange between aforementioned aeroengine components is realized by mixed boundary.

The impingement property under a typical working condition (3000 m altitude) is analyzed. The mixed-phase working conditions are illustrated in Table 1. Considering to the 1/8 nose cone model is established, the mass flow is still 1/8 of the original and set to 135 kg/s. The static pressure at the two outlets is 79500 and 79800 respectively. The rotation speed of the nosecone and fan blade is set to 2580 rpm. The diameters for supercooled liquid droplet MVD_d and ice crystal MVD_{ic} are 20 μm and 110 μm, respectively. Total water content (TWC) is 0.6 g/m³, and in the set of cases liquid water content (LWC) are 0.4 g/m³, 0.3 g/m³ and 0.2 g/m³.
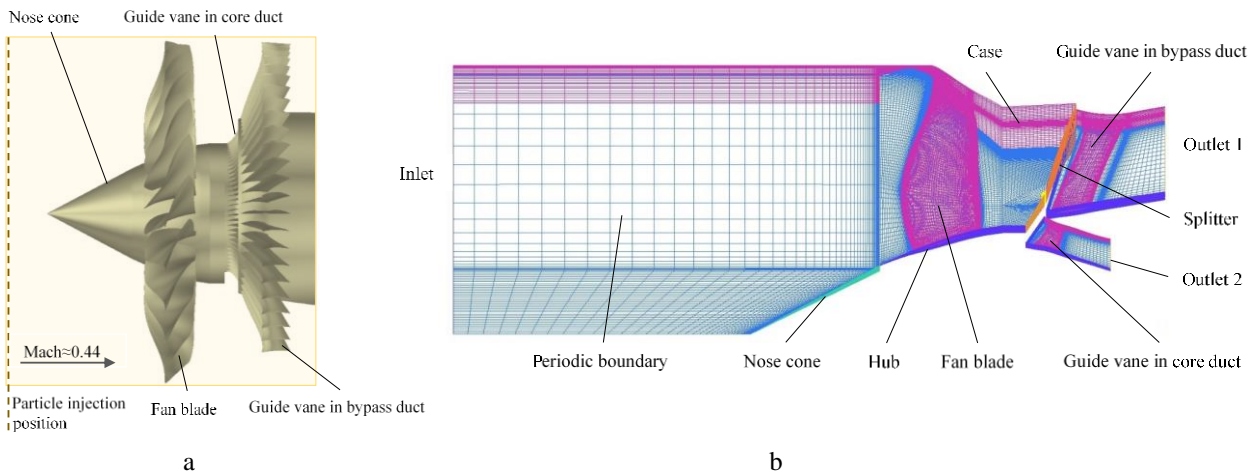

Fig. 1 Aeroengine model: a – geometry components, b – grid models

The characteristics of particle impingement under mixed-phase conditions are analysing by FENSAP-ice, a state-of-art numerical software in aircraft icing field. In the calculation of air flow field, the turbulence model is selected as Spalart-Allmaras one-equation turbulence model.

Table 1

Mixed-phase working conditions

Condition	Case1	Case2	Case3
Inlet mass flow (kg/s)	135	135	135
Inlet total temperature (K)	266	266	266
Outlet static pressure 1 (Pa)	79500	79500	79500
Outlet static pressure 2 (Pa)	79800	79800	79800
Fan speed (rpm)	2580	2580	2580
MVD_d (μm)	23	23	23
MVD_{ic} (μm)	110	110	110
LWC (g/m^3)	0.4	0.3	0.2
ICC (g/m^3)	0.2	0.3	0.4

4. Numerical Results and Discussion

To validate the established numerical model, the collection efficiencies of droplets on fan blade between Case 2 in this simulation and the literature [23] are compared, as shown in Fig 2. Collection efficiency reflects the probability of particles impinging on the surface. It is an important parameter for calculating ice accretion, and is one of the key indicators of the distribution and severity of surface icing. The collection efficiency of droplets in the numerical simulations is agree extremely well with results in the literature, thus validating the accuracy of established numerical model.

Moreover, it is worth to note that the collection coefficient of ice crystals is significantly higher than that of droplets, as illustrated in Fig. 2. It is because that the inertial force of an ice crystal with a larger diameter is much greater than that of a droplet, making it more difficult to alter the original trajectory under the action of aerodynamic force. Consequently, ice crystals are more likely to impact the fan blade surface than droplets. Fig. 3 illustrates velocity vectors and streamlines of droplets and ice crystals near nose cone's surface flow field, further revealing the differences in collection efficiency. As shown in Fig. 3, unlike droplets, ice crystals are less likely to change their trajectory and are prone to be collected by the nose cone surface due to their greater inertial force.

In the three simulation cases, although the total water content remains constant, that is 0.6 g/m^3, the melt ratios, defined as MR=LWC/TWC vary. Fig. 4 shows the mass caught contours for different melt ratios. Mass caught indicates the mass flux of particles that impact on the surface of the model. It is worth to note that as melt ratio increases, the mass flux of particles becomes more concentrated. There is almost no mass caught on the convex side of the fan blade, except for the sweep-forward part where a few particles impinge on. However, the mass flux of particles enriches in a narrow area near leading edge on the convex side of guide vane in bypass and cone duct. The enriched mass flux decreases with a decreasing melt ratio.

Figs. 5 and 6 present the collection efficiency contours for droplets and ice crystals on the concave side of the fan blade and the convex side of the guide vane in bypass duct, respectively. As shown in Fig. 5, droplets and ice crystals primarily impinge on the leading edge on the concave side of the fan blade. Due to their larger inertial force, ice crystals exhibit the more pronounced collection effect and cover a larger wetting area compared to droplets. In contrast, Fig. 6 shows that droplets and ice crystals prone to impinge on the leading edge of the convex side of the guide vane. Meanwhile, ice crystals, influenced by centrifugal force are more likely to pass through the entire structure from the tip of the guide vane in the bypass duct. It is well known that the collection efficiencies of droplets and ice crystals are consistent across the three cases. The variations in the mass caught distributions shown in Fig. 4 can be analysed in terms of the melt ratio (MR) and the further impact of MR on the sticking effect.

Figs. 7 and 8 depict the film thickness contours on the concave side of the fan blade and the convex side of the guide vane in the bypass duct, respectively. In following two sets of figures, as the melt ratio increases, both the film thickness and the wetting limit area expand to some extent. For the fan blade, the maximum film thickness is located
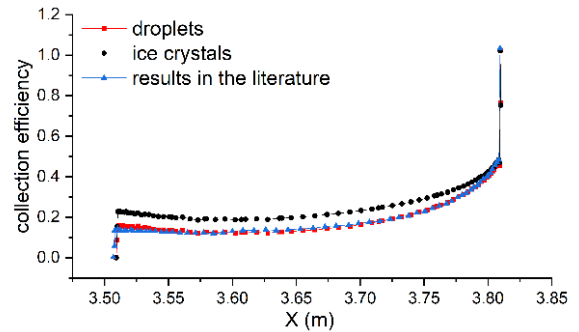
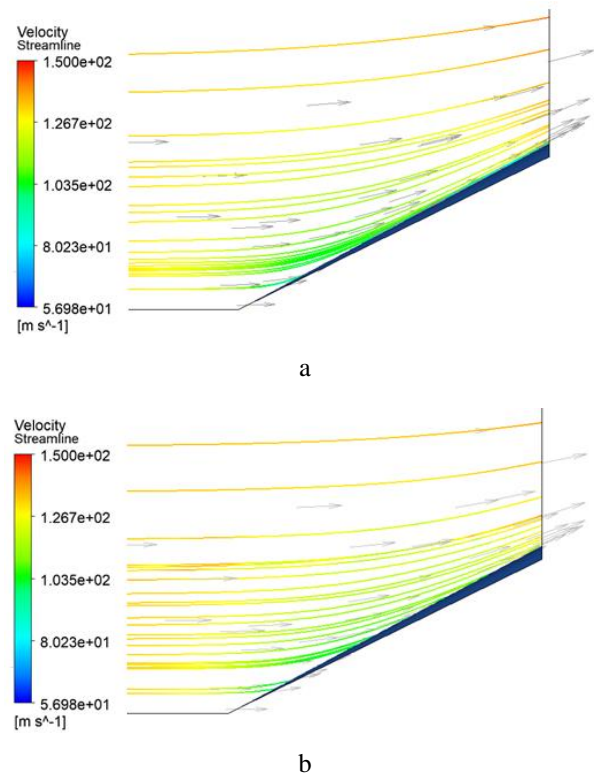Fig. 2 Comparison of particles collection efficiency

a

b

Fig. 3 Velocity vectors and streamlines near nose cone's surface flow field: a – droplet, b – ice crystal
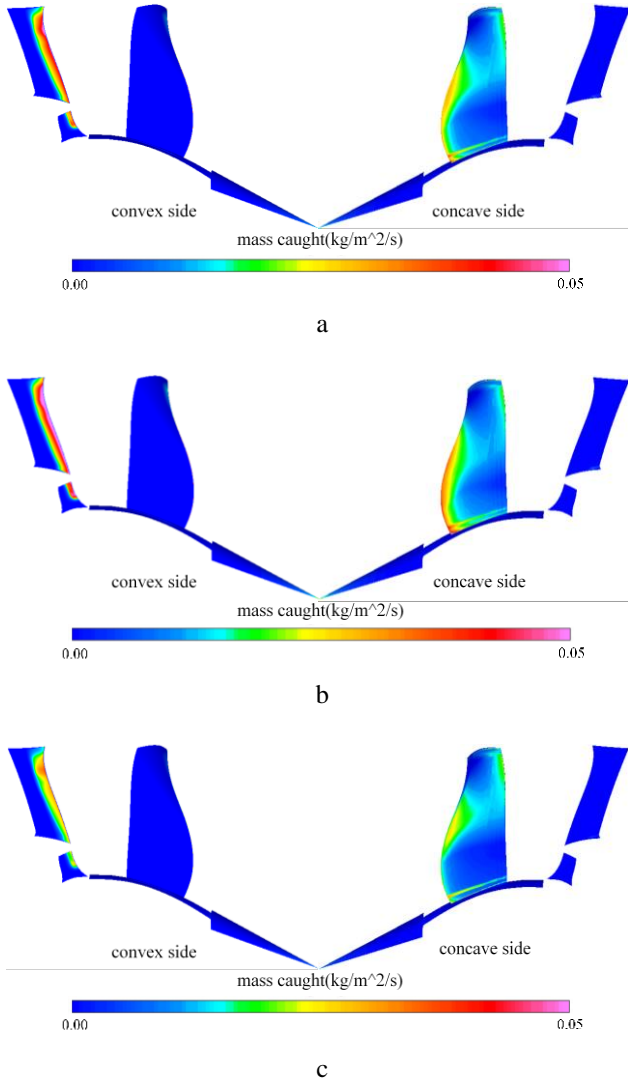
a

b

c

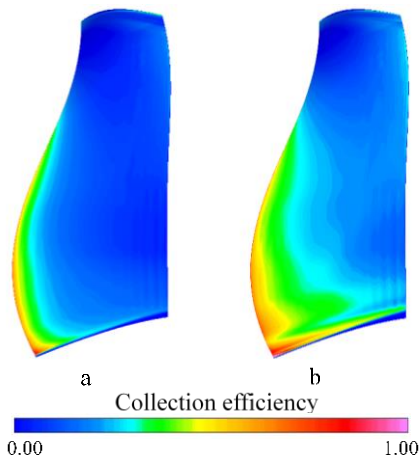Fig. 4 Mass caught contour: a – Case1, b – Case2, c – Case3

Fig. 5 Collection efficiency contour in concave side on fan blade: a – droplet, b – ice crystal
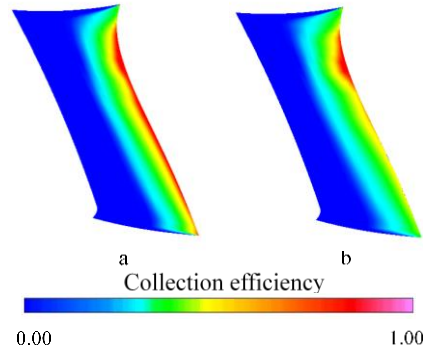

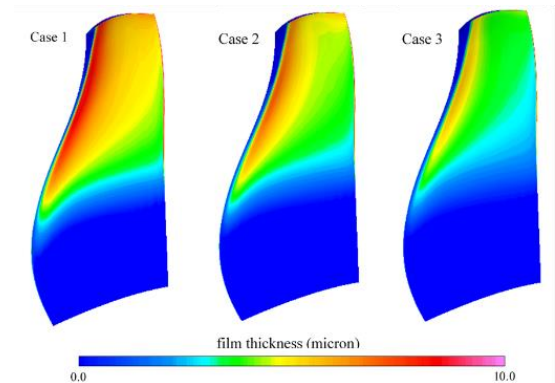Fig. 6 Collection efficiency contour in convex side on guide vane in bypass duct: a – droplet, b – ice crystal

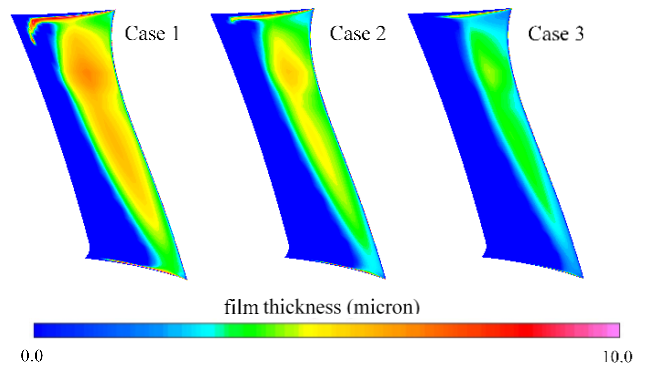Fig. 7 Film thickness contour in concave side on fan blade

Fig. 8 Film thickness contour in convex side on guide vane in bypass duct

near the upper leading edge on the concave side. However, for the guide vane in the bypass duct, due to the stagnation point shifts to the convex side, the location of maximum film thickness moves backward.

Fig. 9 to Fig. 11 compare the film thickness and sticking fraction of ice crystals on different blades and positions, providing further insight into the correlation between film thickness and crystal adhesion effect. As shown in Fig. 9, the film thickness on the middle part of the fan blade, similar to the position in Fig. 2, gradually increases along x-axis due to the increasing collection efficiency of droplets. However, unlike the collection efficiency tendency, the film thickness declines dramatically near the leading edge, perhaps because of the bounce or shatter of droplets with high kinetic energy. The sticking coefficient of ice crystals, subject to inertial force, also decreases sharply in the same region. Meanwhile, as the melt ratio increases, the enrichment of liquid water becomes more significant, and the adhesion of ice crystals becomes more pronounced.

As shown in Figs. 10 and 11, when the impacted surface is sufficiently wet, ice crystals get adhered by the water film, while in area with no overflow water ice crystals will bounce or shatter without sticking. As the melt ratio increases, both the film thickness and the wetting limit get extended correspondingly, result in the maximum sticking
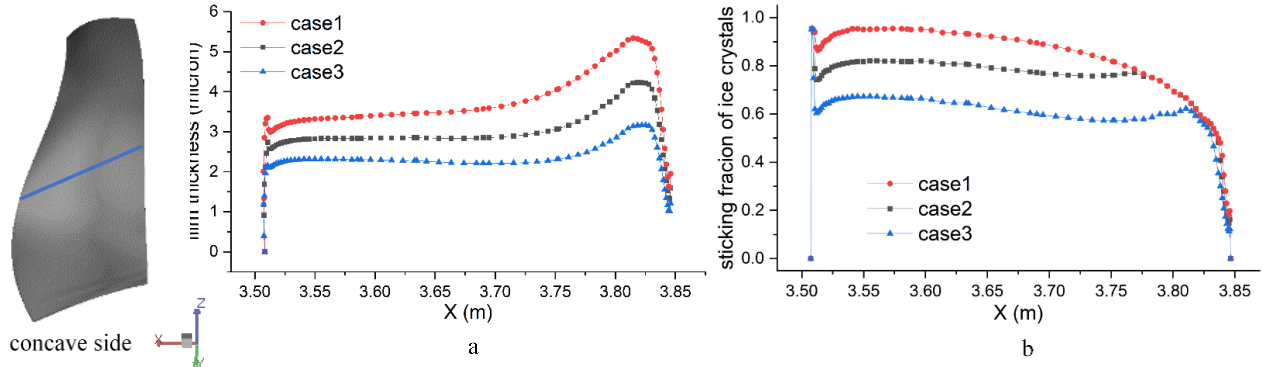
Fig. 9 Comparison on middle part of fan blade: a – film thickness, b – sticking fraction
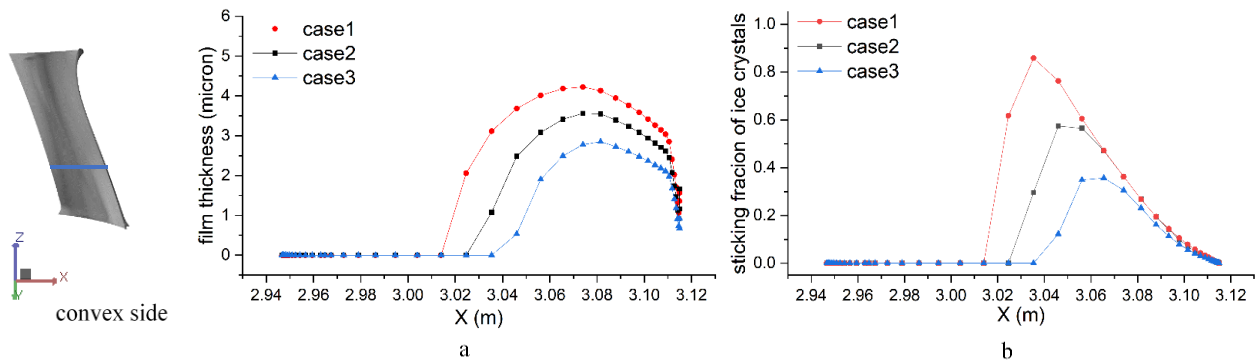

Fig. 10 Comparison on upper part of guide vane in bypass duct: a – film thickness, b – sticking fraction
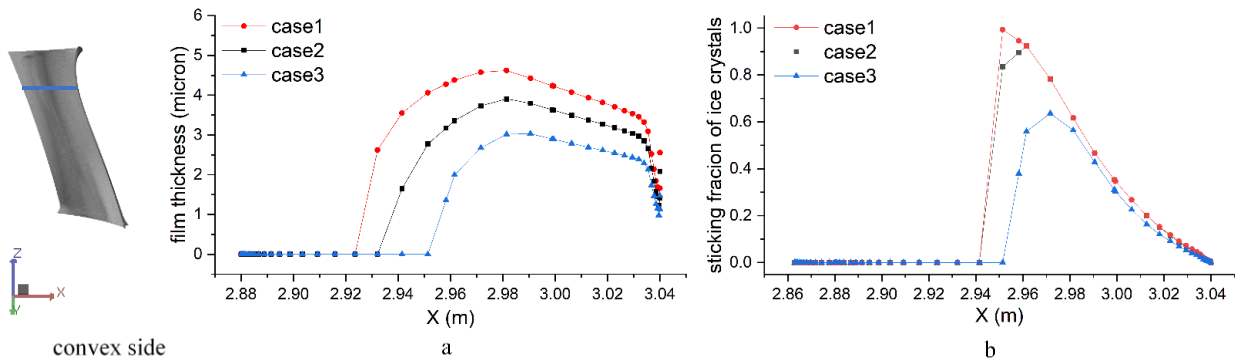

Fig. 11 Comparison on lower part of guide vane in bypass duct: a – film thickness, b – sticking fraction

fraction shifting backward. Compared to lower position, liquid water is more likely to concentrate to upper position and reach a larger wetting limit. Meanwhile, most ice crystals are subjected to centrifugal force, leading to a dramatic drop in the sticking coefficient of ice crystals. Additionally, this cliff-like effect is more pronounced in the upper part of the guide vane due to the greater centrifugal force.

5. Conclusions

In this approach, considering to ice crystal sticking effects, a numerical model was established to solve the particle impingement property of a large by-pass ratio aeroengine under mixed-phase icing conditions. The collection efficiencies of droplets and ice crystals were compared between simulation results and existing literature, demonstrating high accuracy and consistency.

The results showed that the collection efficiency of ice crystals was found to be significantly higher than that of droplets due to the greater inertial force of larger ice crystals, which makes them less susceptible to trajectory changes under aerodynamic forces. Higher melt ratios resulted in a more concentrated mass caught of particles. This phenomenon was particularly noticeable near the concave side of the fan blade and the leading edges of the convex sides of the guide vanes. Increased melt ratios also led to thicker water films and expanded wetting limits on the surfaces. The maximum film thickness locations varied between the fan blade and the guide vane in the bypass duct due to differences in stagnation point positions. Moreover, the adhesion of ice crystals was influenced by the presence of a water film. Higher melt ratios extended the wetting limits and increased the maximum sticking fractions.

These insights are helpful for understanding ice accretion mechanisms in aeroengine bypass ducts and can inform the design of anti-icing and de-icing systems to enhance aircraft safety and performance.

Acknowledgements

References

1. **Cao, Y. H.; Huang, J. S.; Yin, J.** 2016. Numerical simulation of three-dimensional ice accretion on an aircraft wing, International Journal of Heat and Mass Transfer 92: 34-54.
https://doi.org/10.1016/j.ijheatmasstransfer.2015.08.027.

2. **Mason, J. G.; Strapp, J. W.; Chow, P.** 2006. The Ice Particle Threat to Engines in Flight, AIAA 2006-206. 44th AIAA Aerospace Sciences Meeting and Exhibit.
https://doi.org/10.2514/6.2006-206.

3. **Mason, J. G.; Chow, P.; Fuleki, D. M.** 2011. Understanding Ice Crystal Accretion and Shedding Phenomenon in Jet Engines Using a Rig Test, ASME Journal of Engineering for Gas Turbines and Power, 133(4): 041201.
https://doi.org/10.1115/1.4002020.

4. **Yuan, Q. H.; Fan, J.; Bai, G. Z.** 2018. A Review of Ice Crystal Icing in Aero-Engines, Propulsion Technology 39(12): 2641-2650.
https://doi.org/10.13675/j.cnki.tjjs.2018.12.001.

5. **Struck, P. M.; Currie, T.; Wright, W. B.; Knezevici, D. C.; Fuleki, D.; Broeren, A.; Vargas, M.; Tsao, J. C.** 2011. Fundamental Ice Crystal Accretion Physics Studies, SAE 2011-38-0018.
https://doi.org/10.4271/2011-38-0018.

6. **Currie, T.; Struck, P. M.; Tsao, J. C.; Fuleki, D.; Knezevici, D.** 2012. Fundamental Study of Mixed-Phase Icing with Application to Ice Crystal Accretion in Aircraft Jet Engines, AIAA 2012-3035, 4th AIAA Atmospheric and Space Environments Conference.
https://doi.org/10.2514/6.2012-3035.

7. **Currie, T.; Fuleki, D.; Mahallati, A.** 2014. Experimental Studies of Mixed-Phase Sticking Efficiency for Ice Crystal Accretion in Jet Engines, AIAA 2014-3049, 6th AIAA Atmospheric and Space Environments Conference.
https://doi.org/10.2514/6.2014-3049.

8. **Al-Khalil, K.; Irani, E.; Miller, D.** 2003. Mixed Phase Icing Simulation and Testing at the Cox Icing Wind Tunnel, AIAA-2003-0903 41st Aerospace Sciences Meeting and Exhibit.
https://doi.org/10.2514/6.2003-903.

9. **Knezevici, D. C.; Fuleiki, D.; Currie, T.; MacLeod, J.** 2012. Particle Size Effects on Ice Crystal Accretion, AIAA 2012-3039 4th AIAA Atmospheric and Space Environments Conference.
https://doi.org/10.2514/6.2012-3039.

10. **Hauk, T.; Roisman, I.; Tropea, C.** 2014. Investigation of the Impact Behaviour of Ice Particles. AIAA 2014-3046 6th AIAA Atmospheric and Space Environments Conference.
https://doi.org/10.2514/6.2014-3046.

11. **Hauk, T.** 2016. Investigation of the Impact and Melting Process of Ice Particles. Darmstadt: Technische Universität Darmstadt, Available from Internet:
https://tuprints.ulb.tu-darmstadt.de/5280.

12. **Villedieu, P. A.; Trontin, P.; Chauvin, R.** 2014. Glaciated and mixed-phase ice accretion modeling using ONERA 2D icing suite, AIAA-2014-2199 6th AIAA Atmospheric and Space Environments Conference.
https://doi.org/10.2514/6.2014-2199.

13. **Trontin, P.; Blanchard, G.; Villedieu, P. A.** 2016. Comprehensive numerical model for mixed-phase and glaciated icing conditions, AIAA 2016-3742 8th AIAA Atmospheric and Space Environments Conference.
https://doi.org/10.2514/6.2016-3742.

14. **Trontin, P.; Blanchard, G.; Kontogiannis, A.; Villedieu, P.** Description and assessment of the new ONERA 2D icing suite IGLOO2D, AIAA 2017-3417. 9th AIAA Atmospheric and Space Environments Conference.
https://doi.org/10.2514/6.2017-3417.

15. **Norde, E.; van der Weide, E. T. A.; Hoeijmalers H. W. M.** 2018. Eulerian Method for Ice Crystal Icing, AIAA Journal, 56(1): 222-234.
https://doi.org/10.2514/1.J056184.

16. **Zhang, L. F.; Liu Z. X.; Zhang, M. H.** 2016. Numerical simulation of ice accretion under mixed-phase conditions, Proceedings of the Institution of Mechanical Engineers, Part G: Journal of Aerospace Engineering 230(13): 2473-2483.
https://doi.org/10.1177/0954410015626734.

17. **Bu X. Q.; Li H.; Huang P.; Lin, G.** 2021. Numerical simulation of mixed phase icing on two-dimensional airfoil, Acta Aeronautica et Astronautica Sinica 41(12): 124085 (in Chinese).
https://doi.org/10.7527/S1000-6893.2020.24085.

18. **Qi, H.; Chang, S. N.; Yang Y.; Chang, P.** 2024. Numerical investigations on aero-engine icing characteristics at mixed phase conditions, Applied Thermal Engineering 238: 122044.
https://doi.org/10.1016/j.applthermaleng.2023.122044.

19. **Currie T.; Fuleki, D.; Davison, C.** 2015. Simulation of Ice Particle Melting in the NRCC RATFac Mixed-Phase Icing Tunnel. SAE 2015 international Conference on Icing of Aircraft, 2015-01-2107.
https://doi.org/10.4271/2015-01-2107.

20. **Baumert, A.; Bansmer, S.; Trontin, P.; Villedieu, P.** 2018. Experimental and numerical investigations on aircraft icing at mixed phase conditions, International Journal of Heat and Mass Transfer 123: 957-978.
https://doi.org/10.1016/j.ijheatmasstransfer.2018.02.008.

21. **Bartkus, T. P.; Struck, P. M.; Tsao, J. C.; Van Zante, J. F.** 2016. Numerical Analysis of Mixed-Phase Icing Cloud Simulations in the NASA Propulsion Systems Laboratory, AIAA 2016-3739. 8th AIAA Atmospheric and Space Environments Conference.
https://doi.org/10.2514/6.2016-3739.

22. **Nilamdeen, S.; Habashi, W. G.** 2011. Multiphase approach toward simulating ice crystal ingestion in jet engines, Journal of Propulsion and Power 27(5): 959-969.
https://doi.org/10.2514/1.B34059.

23. **Tan, Y.; Wei, W. G.** 2020. Numerical Study of Super-Cooled Droplet Impingement on Aeroengine, Mechanika 26(1): 35-40.
https://doi.org/10.5755/j01.mech.26.1.23107.

Q. Guo, J. Du, F. Qian, N. Ding

NUMERICAL STUDY OF PARTICLE IMPINGEMENT
ON AEROENGINE UNDER MIXED-PHASE
CONDITIONS

S u m m a r y

In this approach, considering the effects of ice crystal adhesion, a numerical model was developed to analyze the particle impingement characteristics of a large bypass ratio aeroengine under mixed-phase icing conditions. The collection efficiency of droplets obtained by the proposed model shows excellent agreement with existing literature. Additionally, the collection efficiency of ice crystals is significantly higher than that of droplets, due to their greater inertial force. The mechanism of liquid film acting on the ice crystal adhesion affect was investigated. It was found that a higher melt ratio leads to more abundant liquid water and a more extensive wetting area, significantly enhancing the capability to stick ice crystals. Furthermore, due to the influence of centrifugal force on ice crystals, the sticking coefficient of ice crystals exhibits a dramatic decrease. This cliff-like drop in the sticking coefficient becomes more pronounced with greater centrifugal force.